

Longitudinal analysis of traumatic brain injury using
semi-automatic multimodal segmentation of MR images

Andrei Irimia, PhD¹, Micah C. Chambers, MS^{1,2}, Jeffrey R Alger, PhD^{3,4,5}, Maria Filippou, MD⁶, Marcel W Prastawa, PhD^{7,8}, David A Hovda, PhD³, Guido Gerig, PhD^{7,8}, Arthur W Toga, PhD^{1,4,5}, Ron Kikinis, MD⁹, Paul M Vespa, MD, FCCM, FAAN⁶, John D Van Horn, MEng, PhD¹

¹Laboratory of Neuro Imaging, Department of Neurology, University of California, Los Angeles, CA 90095

²School of Engineering and Applied Science, University of California, Los Angeles, CA 90095

⁶Department of Radiological Sciences, University of California, Los Angeles, CA 90095

⁷Brain Research Institute, Department of Neurology, University of California, Los Angeles, CA 90095

⁸Division of Brain Mapping, Neuropsychiatric Institute, University of California, Los Angeles, CA 90095

³Brain Injury Research Center, Departments of Neurosurgery and Neurology, University of California, Los Angeles, CA 90095

⁴Scientific Computing and Imaging Institute, University of Utah, Salt Lake City, UT 84112

⁵School of Computing, University of Utah, Salt Lake City, UT 84112

⁹Surgical Planning Laboratory, Department of Radiology, Harvard Medical School, Boston, MA 02115

Abstract

Though neuroimaging is essential for prompt and proper management of TBI, there is regrettable and acute lack of robust methods for the visualization and assessment of TBI pathophysiology, especially for the purpose of improving clinical outcome metrics. Until now, the application of automatic segmentation algorithms to TBI in a clinical setting has remained an elusive goal because existing methods have, for the most part, been insufficiently robust to faithfully capture TBI-related changes in brain anatomy. This article introduces and illustrates the combined use of multimodal TBI segmentation and longitudinal analysis using 3D Slicer, a widely-used software environment whose TBI data processing solutions are openly available. For three representative TBI cases, semi-automatic tissue classification and 3D model generation are performed to assess longitudinal TBI evolution using multimodal volumetrics and clinical atrophy measures. Identification and quantitative assessment of extra- and intra-cortical bleeding, lesions, edema and diffuse axonal injury are demonstrated. The proposed tools allow cross-correlation of multimodal metrics from structural imaging (structural volume, atrophy measurements, etc.) with clinical outcome variables (time since injury, age, gender, etc.) and other potential factors predictive of recovery. In addition, the workflows described are suitable for TBI clinical practice and patient monitoring, particularly for assessing damage extent and for the measurement of neuroanatomical change over time. With knowledge of general location, extent, and degree of change, such metrics can be associated with clinical measures and subsequently used to suggest viable treatment options for individual subjects against patterns that are typical TBI populations. Thus, the methodology demonstrated here using the 3D Slicer platform has the potential for significant impact upon the state of the art in TBI neuroimaging as well as upon the added benefit of TBI neuroimaging techniques from the standpoint of clinical monitoring, diagnosis and treatment.

Introduction

With an estimated 1.7 million Americans sustaining a traumatic brain injury (TBI) every year (Faul M. 2010), the magnitude of this medical concern to the US cannot be overstated (Chen and D'Esposito 2010). Every year, TBI cases are associated with 1.2 million emergency room visits and over 50,000 deaths (Langlois). Interest in and public awareness of TBI-caused diffuse axonal injury (DAI) has surged with the publication of studies suggesting that DAI in professional and amateur athletes may have both acute and chronic effects upon neurocognitive function (De Beaumont, Theoret et al. 2009). Moreover, the large number of recent TBI cases in soldiers returning from military conflicts has created a significant clinical challenge for US Veterans Administration hospitals (Taber, Warden et al. 2006) and has highlighted the critical need for improvement in TBI care and treatment.

Prompt and proper management of TBI sequelae can significantly alter their course, improve mortality and morbidity, reduce hospital stay and decrease health care costs (Watts, Hanfling et al. 2004). Neuroimaging of TBI is thus vital for surgical planning by providing important information for anatomic localization and surgical navigation, as well as for guiding decisions regarding the aggressiveness of TBI treatment (Chesnut 1998). Moreover, because TBI often results in characteristic impairments dependent on the area of involvement (Warner, Marquez de la Plata et al. 2010), lesion analysis can assist in the localization of cognitive processes and in the attempt to obtain novel information on the relationship between brain anatomy and behavior (Bates, Wilson et al. 2003). For all these reasons, reliable and precise methods of TBI assessment can play an essential role during both acute and chronic therapy of this condition.

Whereas neuroimaging is often critical for proper TBI clinical care, there is regrettable and acute lack of robust methods for the exploration, visualization and quantitative assessment of TBI-related anatomical insults and pathophysiology. Starting 2-3 days after the acute injury, magnetic resonance imaging (MRI) is generally considered to be superior to computed tomography (CT) for the purpose of TBI assessment and analysis. Whereas CT is better at detecting the pathology of bones and certain bleeds, MRI can identify bleeds more easily as blood composition gradually changes following TBI (Dubroff and Newberg 2008). In this context, the application of automatic MRI segmentation algorithms to the clinical investigation of TBI cases remains an elusive goal because many existing methods are insufficiently robust to accurately capture TBI-related changes in brain anatomy. Thus, because the state of the art in quantitative MRI analysis of TBI often involves labor-intensive manual tissue classification, the clinician's ability to generate robust and accurate three-dimensional (3D) models of neuropathology for TBI diagnosis and treatment remains extremely limited. Consequently, despite recent progress in the development of robust image analysis tools, it remains difficult to quantify TBI-related brain insults both uni- and multi-modally, particularly for the purpose of improving clinical outcome metrics.

To address the urgent need for clinician-friendly TBI analysis tools, we here propose and illustrate the combined use of multimodal, semi-automatic TBI analysis methods within 3D Slicer, a freely available software environment for the segmentation, registration, visualization and quantification of MR images. In contrast with many other segmentation environments for TBI that have appeared in the literature (Ding, Marquez de la Plata et al. 2008), the 3D Slicer environment is both freely available as well as widely used by clinicians, scientists and engineers. Consequently, the segmentation and visualization methodology demonstrated here has the potential to significantly impact the field of TBI neuroimaging, possibly leading to a paradigm shift whose prospective impact is difficult to dismiss. To showcase the ability to perform quantitative longitudinal analysis of TBI in 3D Slicer, we present three

cases of semi-automatic TBI volume segmentation and 3D brain model generation while also highlighting the added clinical insight which this workflow can offer.

Subjects and Methods

Research Participants and MRI Acquisition

Anonymized neuroimaging data from three representative TBI subjects were acquired at the Brain Injury Research Center of the UCLA Geffen School of Medicine. The study and data acquisition protocol were designed and carried out in accordance with the Declaration of Helsinki and were approved by the UCLA Institutional Review Board. Signed informed consent was obtained from each patient or from their legally authorized representative before any procedures were performed. In Table 1, the age, sex and types of MR scans acquired from each patient are specified in addition to the number of days after injury when the acute and chronic scan sessions took place. For example, the first patient is a 45-year old male suffering from blunt trauma who was scanned 2 and 176 days post-injury (acute and chronic sessions, respectively). In the case of the first two subjects, the sequences being used are representative of MR acquisition protocols that are appropriate for patients requiring critical care. In the case of patient 3, we illustrate the use of an extended MR scan protocol involving 12 distinct sequence types. This protocol requires significantly more acquisition time and can be envisioned as applicable for TBI patients in highly stable condition and/or who can withstand remaining motionless in the MR scanner for the extended amount of time required for the acquisition of images. In the context of this study, illustration of both protocols is useful because it can demonstrate the ability of our segmentation environment to accommodate, on the one hand, the use of a limited number of scan types and, on the other hand, the additional amount of clinically-relevant information being supplied by a more enhanced protocol. Throughout the paper, the set of 5 sequences that were used for the imaging of the first two patients are referred to as the 'standard' protocol, whereas the set of 12 sequences used in the third patient is referred to as the 'extended' protocol.

MR volumes were acquired at 3 T from each subject using a Siemens Trio TIM scanner (Siemens AG, Erlangen, Germany). To eliminate the effect of different scanner parameters during each scanning session, every subject was scanned using the same scanner for both acute and chronic time points. The MP-RAGE sequence (Mugler and Brookeman 1990) was used to acquire T1-weighted images. In addition, MR data were also acquired using fluid-attenuated inversion recovery (FLAIR, (De Coene, Hajnal et al. 1992)), T2-weighted turbo spin echo (TSE, also known as fast spin echo, FSE, (Jones, Mulkern et al. 1992)), gradient-recalled echo (GRE) T2-weighted images as well as susceptibility weighted imaging (SWI, (Sehgal, Delproposto et al. 2005)). In the case of the enhanced acquisition protocol for Patient 3, 7 additional scan sequences were also employed, including diffusion weighted imaging (DWI), diffusion tensor imaging (DTI), and maximum intensity projection (mIP). A complete list of these sequences is provided for each patient in table 1, while Table 2 specifies standard MR parameters associated with each sequence.

Identification of pathology

TBI comprises a variety of cerebral lesion types, including hematoma, subarachnoid hemorrhage, contusion and DAI. TBI edema, in particular, can further be characterized by its extent and distribution ranging from perifocal (regional) to diffuse (generalized) (Unterberg, Stover et al. 2004). In this study, non-hemorrhagic lesions on MRI scanning were coded as hyperintensities on FLAIR images. By using a long inversion time (TI), the FLAIR sequence achieves high contrast between lesions and both healthy tissue as well as cerebrospinal fluid (CSF). In this type of neuroimaging, lesions appear as hyperintense regions in the white matter (WM), surrounded by normal tissue of lower, more uniform intensity (Itti,

Chang et al. 2001). On the other hand, T2-weighted GRE imaging is excellent for the detection of acute hemorrhagic lesions, and SWI is much more sensitive than conventional T2-GRE in detecting hemorrhagic DAI. By comparison, the sensitivity of DWI to identify DAI lesions is similar to that of FLAIR, and inferior to that of T2-GRE for detecting hemorrhage (Huisman 2003). Although GRE images do reveal some microhemorrhages, this sequence is poor at resolving between gray matter (GM) and lesions, on the one hand and WM and lesions, on the other hand, at least partly because GM lesions have higher relaxation times than those of normal WM. For all these reasons, brain lesions adjacent to CSF were segmented from volumes acquired using FLAIR, and the quality of the segmentations obtained was confirmed using GRE imaging. TSE T2-weighted volumes were also used to confirm lesion characterization, and DWI volumes were examined, where available, to additionally distinguish vasogenic (increased diffusion) from cytotoxic (restricted diffusion) edema (Warach, Gaa et al. 1995; Huisman, Sorensen et al. 2003). Non-hemorrhagic shearing lesions were defined as hyperintense lesions that were visible primarily on T2-weighted or FLAIR images. This method of identification was adopted because some shearing lesions often do not show substantial amounts of hemorrhage but are primarily visible as areas of hyperintensity on FLAIR, T2-weighted and GRE images.

The appearance of hemorrhages in MR imaging is highly variable across sequences (Greenberg, Vernooij et al. 2009), as it depends on a number of variables, both intrinsic (hemoglobin oxygenation, erythrocyte integrity) and extrinsic (scanner field strength, receiver bandwidth, T1 or T2 weighing, etc.). Because SWI takes into account MR signal phase information, regional magnetic field alterations due to iron concentration gradients in the brain are easier to capture with this technique. As a result, SWI sequences are very useful in TBI imaging because susceptibility effects make microhemorrhages more obvious in SWI compared to other paradigms. Because SWI is thus generally superior to GRE and T2-weighted imaging to detect hemorrhagic lesions (Tong, Ashwal et al. 2003), volumes acquired using this former modality were used to identify micro-hemorrhages that were poorly detectable or undetectable using other sequences. Specifically, following previous guidelines (Tong, Ashwal et al. 2003), hemorrhagic lesions were defined as hypointense foci that were not compatible with vascular, bone, or artifactual structures on conventional GRE images. Whenever foci etiology was doubtful, the lesions in question were not considered to be hemorrhagic.

In summary, image segmentation and model generation was performed in all three patients using the standard protocol defined previously. In the case of Patient 3, images that were additionally available in the context of the extended protocol were also used to confirm segmentation accuracy as well as to illustrate the additional capabilities of our environment to segment images from a variety of MR data sets and combination of sequences.

Image Processing

Because TBI involves injury to both neuronal cell bodies and axonal processes, global atrophy of GM and WM are both common in this condition. Partly for this reason, reliable segmentation of WM and GM lesions is necessary for accurate quantitative analysis of TBI lesions. Additionally, accurate quantification of total lesion volume (lesion load) is essential for longitudinal analysis of TBI. To address these clinical needs, we employed the semi-automatic segmentation tools available in 3D Slicer software, including the Atlas Based Classification (ABC) and Expectation Maximization (EM) segmenters, which have been described elsewhere (Pohl, Bouix et al. 2007; Zoellei 2007; Prastawa 2008) and used widely to detect pathology in MR scans (Prastawa, Bullitt et al. 2009). Briefly, the ABC algorithm can perform multimodal registration of MR images (Maes, Collignon et al. 1997), tissue classification of the brain (Van Leemput, Maes et al. 1999), as well as lesion segmentation based on outlier detection (Prastawa, Bullitt et al. 2004) and physical model estimation (Prastawa, Bullitt et al. 2003; Prastawa 2008). The EM Segmenter,

on the other hand, is an algorithm guided by prior information represented algorithmically within a tree structure to estimate optimal segmentation via a conventional classifier. In this latter case, the tree mirrors the hierarchy of anatomical structures and the subtrees correspond to limited segmentation problems (Pohl, Bouix et al. 2007).

As opposed to other specialized segmenters to which access is often restricted from outside users, both ABC and EM segmenters are freely available as segmentation modules in 3D Slicer. Both methods are automatic and their executions require minimal user supervision. In addition, the ABC segmenter possesses the ability to perform co-registration of an arbitrary number of MR volumes acquired using various sequences. This makes it highly suitable to the present multimodal TBI imaging paradigms, where as many as 12 distinct sequence types are employed. Before segmentation, all image volumes were co-registered to the pre-contrast MP-RAGE T1-weighted volume acquired during the acute baseline scanning session. Intensity normalization within and between scans was performed within 3D Slicer. Bias field correction was applied using a fourth-order polynomial model. Because the anatomy of severe TBI often diverges from healthy anatomy to a very large extent, segmentation errors can frequently occur, especially in severe TBI cases. To address this shortcoming, manual review in 3D Slicer by an operator with experience in the recognition of neurotrauma was performed with the purpose of editing and correcting segmentation errors. The guidelines of Filippi et al. (Filippi 1998) for editing and segmentation were followed. Nevertheless, when assessing the extent of segmentation error, it is fair to note that, although often considered to be the gold standard, even manual outlining results in both moderate (3-10%) intra-observer error as well as larger inter-operator variabilities (Raff et al., 2000). In conclusion, it is reasonable to expect the presence of subtle segmentation inaccuracies even in the context of our rigorous segmentation paradigm.

Quantitative Metrics

Tissue-type segmentation was used to calculate the total volume of three selected structure types (ventricular system, non-hemorrhagic lesions, and hemorrhagic lesions). The volume change was computed as the ratio of the difference in volume between the follow-up and acute baseline time points, to the volume at the latter time point. In addition to these measures, we also report five measures of atrophy, namely the bifrontal index (Hahn and Schapiro 1976), the bicaudate index (Earnest, Heaton et al. 1979), Evan's index (Synek, Reuben et al. 1976), the ventricular index (Gyldensted 1977) and Huckman's index (Huckman, Fox et al. 1975).

Let the bifrontal horn distance be the maximum width of the anterior horns of the lateral ventricles (HLV). Then the bifrontal index is the ratio of the maximum HLV width to the inner skull diameter at HLV level. The bicaudate index is defined as ratio of the minimum width of the lateral ventricles (MLV) to the width of the inner skull at that level. Evan's index is the ratio of the HLV to the maximum inner skull diameter (MISD). Finally, the ventricular index is equal to MLV/HLV while Huckman's index is the sum of the MLV and HLV measures.

Results

Because neurotrauma often exhibits multiple, overlapping forms of focal and/or diffuse injury, insight from TBI imaging is greatly enhanced through the use of multimodal techniques. In what follows, the results of each segmentation and 3D model generation are reviewed and the procedures employed to perform tissue classification are illustrated.

Case 1

As Figure 1 reveals, Patient 1 exhibits a large deep-brain injury which is hyperintense in the FLAIR image (Figure 1 (C)) due to perfusion by CSF from the ventricular system. Contralaterally with respect to this injury, a smaller insult in the deep WM is also apparent in T1-weighted, FLAIR and GRE images (Figures 1 (A), (C) and (D), respectively). The posterior portion of the left ventricle seems larger than the corresponding part of the right ventricle, possibly due to local WM inflammation. Additionally, FLAIR seems to reveal some DAI in the area surrounding the primary injury (yellow arrows), while GRE demonstrates the presence of hemorrhage both adjacent to as well as remote from the primary insult (Figure 1 (D), green arrows). Thus, the inclusion of a GRE sequence is particularly useful in this case because DAI can be visualized indirectly through shear hemorrhages caused by blood vessel lesions (Scheid, Preul et al. 2003). Figure 1 suggests that the ability to characterize TBI is greatly enhanced by the use of SWI. As already quantified in detail by other authors (Tong, Ashwal et al. 2003; Tong, Ashwal et al. 2008) and illustrated in Figure 1 (E), this technique is very sensitive in the detection of extravascular blood products, which is illustrated by SWI's identification of significant hemorrhage surrounding the primary injury, as well as diffusely throughout the brain (Figure 1 (E)).

In Figure 2, the results of the TBI segmentation for Patient 1 are shown. Each row displays one of 6 canonical views (left, right, dorsal, ventral, anterior and posterior) of the MR-segmented brain, with every column corresponding to one particular structure type (ventricles, extracortical insults, non-hemorrhagic cortical lesions, hemorrhagic cortical lesions, and the full model). In each image, GM and WM are transparent, whereas the ventricular system is additionally transparent in rows 2-5 to facilitate visualizing the relative position of each structure type with respect to other cortical landmarks. Figure 2 (A) shows 3D views of the ventricular system, with arrows drawing attention to anatomical changes due to pathology. As previously posited based on Figure 1, this volumetric analysis reflects the large extent of the primary injury, as well as the significant amount of bleeding present in the WM. The posterior part of the left ventricle is found to have been slightly enlarged as a consequence of the lesion compressing its anterior portion (Figure 2 (A)). By comparison, the posterior part of the right ventricle appears thinner, although its anterior portion is larger because of the primary insult being located contralaterally with respect to the latter (Figure 2 (C-D)). Figures 2 (C) and (D) also illustrate the large volume of the primary injury, which covers a large spatial extent mainly in the left hemisphere and extends from the inferior to the superior extremity of the brain.

In Figure 2 (E), standard views of the full 3D segmentation model are shown where all structures are visible, with the exception of the WM and GM models, which are omitted for visual clarity. Because the 3D model of subdural edema obstructs the view, comprehensive evaluation of TBI-related pathology is not possible from analysis of the full model. Nevertheless, this perspective does have the advantage of allowing one to visualize and summarize all forms of TBI-related pathology as displayed in the other columns.

Figure 3 displays the segmentations of volumes acquired from Patient 1 during the chronic follow-up session. Although the ventricular system appears to exhibit improved bilateral symmetry (Figure 3 (A)) and the combined volume of bleeds as extracted from GRE and SWI imaging appears to be much smaller than in the acute scan (Figure 3 (C)), the latter cannot be stated regarding the volume of the scar due to the primary injury (Figure 3 (B)). In fact, the volume of the lesion does not appear to have decreased appreciably at follow-up. This is confirmed in Figure 4, where a visual longitudinal analysis of the volumes associated with each structure is performed. For the purpose of the latter, all lesions in the acute baseline volume (whether hemorrhagic or non-hemorrhagic) are displayed jointly in red, whereas

the lesions and bleeds at follow-up are shown in green. This avoids the highly problematic task of differentiating lesions in the follow-up model according to their provenience (i.e. from hemorrhagic or non-hemorrhagic regions in the acute baseline model), while still allowing one to perform a visual and quantitative comparison of the two time points.

In Figure 4, results of the longitudinal analysis for Patient 1 are displayed. The left view of the GM volume reveals important decrease in inflammation at the follow-up time point, particularly over dorsolateral frontal, prefrontal, parietal and over superior temporal cortex. Comparison of the acute and chronic WM volumes, on the other hand, suggests substantial decrease in inflammation over the entire frontal and prefrontal cortex, as well as more diffusely over the other cortical lobes. In this subject, comparison of the volumes associated with lesions portrays the acute baseline lesions as encasing those imaged at the chronic follow-up time point, which again suggests substantial decrease in injury extent. The longitudinal analysis in Figure 4 suggests that Patient 1 exhibits only a small longitudinal change in the volume of the ventricular system. This is confirmed by the quantitative analysis reported in Table 3, where it is seen that there is only a 1.3% increase in ventricular volume between the acute and chronic time points. By contrast, in agreement with Figure 4, both hemorrhagic and non-hemorrhagic lesions are found to decrease in volume substantially, i.e. by over 76%. Among the metrics used for quantification of atrophy, Evan's index registers the largest percentage change (11.42%) from the acute to the chronic time point.

Case 2

Whereas Patient 1 illustrates the effects of a large WM lesion caused by a blunt, closed-head trauma, the imaging of Patient 2 illustrates the damage to the brain caused by a gunshot wound. In this latter case, all imaging modalities reveal extensive—both focal and diffuse—injuries in the left hemisphere, with particularly obvious damage to the temporal lobe, both laterally and medially (Figure 5). In addition, all modalities reveal injuries to the cerebellum and brain stem, with FLAIR showing large portions of these structures being perfused by CSF (Figure 5 (C)). The medial aspect of the right temporal lobe as imaged using FLAIR and GRE T2 suggests the existence of an insult in this structure as well. In the acute scan slices displayed, the size and extent of the primary injury make the left ventricle essentially indiscernible. All modalities hint to the presence of extensive extracortical insults, while GRE T2-weighted and SWI images demonstrate the presence of significant hemorrhage (Figures 5 (D-E)). The images acquired during the chronic scan session illustrate significant left ventricular hypertrophy, presumably due to WM loss, while GM loss is also obvious, especially as seen on the lateral aspect of the left temporal lobe.

In Patient 2, the segmentations of the MR volumes acquired during the acute TBI scan (Figure 6) reveal the presence of substantial loss of volume in the left ventricle as well as notable extracortical insults. Both hemorrhagic and non-hemorrhagic cerebral lesions are found to cover large portions of the temporal lobe, with some injuries also being present dorso-frontally in the left hemisphere as well as in the periventricular region of the anteromedial right hemisphere. The segmentation of the MR data set acquired at follow-up (Figure 7) confirms that Patient 2 exhibits significant enlargement of the lateral ventricle ipsilateral to the primary insult, with large portions of the ventrolateral temporal lobe exhibiting low-density, CSF-perfused tissue (Figure 7 (B)).

Longitudinal analysis of the GM volume in this subject hints to significant lateral shift of the longitudinal fissure (Figure 8 (A), dorsal view), substantial decrease in frontal lobe GM volume as a consequence of decreased inflammation (Figure 8 (A), right and left views), and large decrease in left temporal lobe lesion size (Figure 8 (A), ventral view) amounting to a non-hemorrhagic lesion volume that is 63.6%

smaller than that at the acute baseline time point (Table 3). Comparison of the ventricular system between acute baseline and chronic follow-up (Figure 8 (C)) confirms the significant increase in volume of the left ventricle and decrease in volume of the right ventricle. Whereas the former is probably due to the replacement of injured WM by CSF, the latter is possibly due, at least in part, to the decrease in intracranial pressure between the two time points. As summarized in Table 3, the increase is over 50 cm³, which amounts to a 107% increase with respect to the ventricular volume at the acute time point. The obvious lateral shift in the position of the fourth ventricle (Figure 8 (C), anterior and posterior views) appears to confirm the noteworthy finding that the midline has been shifted to the left during the chronic period. This impression is strengthened by the fact that lesion volume is smaller at follow-up compared to baseline (Figure 8 (D)). In Patient 2, the bicaudate and ventricular indices have the largest percentage changes at follow-up compared to baseline (26.89% and 15.15%, respectively).

Case 3

Shown in Figure 9 are MR images acquired from Patient 3. As in the previous patient, one can note an extensive primary TBI covering a significant portion of the left temporal lobe, including the inferior, middle and superior temporal gyri and sulci. Smaller insults include lesions to the frontopolar region of both hemispheres, as well as bilateral subdural edema over substantial lateral portions of the frontal, parietal, temporal and occipital lobes. Insults are visible as hypo-intensities in T1-weighted MP-RAGE images (Figure 9 (A)) and as hyperintensities in T2-weighted TSE images (Figure 9 (B)). FLAIR images (Figure 9 (C)) reveal hyperintense, CSF-perfused lesions located bilaterally in the frontal lobe, as well as a primary insult in the left temporal lobe. Focal and hyperintense periventricular lesions are also visible throughout the volume. Figure 9 (D) presents T2-weighted GRE images, with hypo-intensities present in both the acute baseline and follow-up volumes. In the present case, this type of imaging reveals hypointense, CSF-perfused lesions (Figure 9 (D)) as well as some chronic injuries in proximity to the left ventricle. MR volumes available from the extended protocol (Figure 9 (G-L)) provide confirmation of these findings, with additional identification of micro-bleeds being made possible from the mIP angiography volume, which allows one to identify the existence of numerous additional micro-bleeds throughout the brain (Figure 9 (L)). Oxygen extraction factor (OEF, Figure 9 (H)), DTI images (Figure 9 (I)), and DWI-based apparent diffusion coefficient (ADC) maps (Figures 9 (J-K)) additionally confirm the existence and extent of lesions. Because ADC represents the algebraic sum of vasogenic (increased ADC) and cellular (decreased ADC) brain edema, the ADC maps (Figures 9 (J-K)) can be used to confirm the presence of edemic regions as identified using FLAIR, as well as T1 and T2 images. Whereas mIP (Figure 9 (L)) and DWI (Figure 9 (J-K)) are both useful for the identification of hemorrhage, Figure 9 (E) demonstrates the improved ability of SWI to localize hemorrhages and microbleeds, some of which are not visible using the former two techniques. In addition, SWI is capable of identifying microbleeds present in the follow-up scans (Figure 9 (E), left).

Inspection of the left and right views of the brain as reconstructed in Figure 10 reveals left-right asymmetry of the lateral ventricles, possibly partly due to inflammation. The temporal horn of the left ventricle is positioned slightly above the horizontal plane of the right ventricle (left and right views), and its location is also seen to have shifted more medially (dorsal and ventral views). Figure 10 (B) displays the spatial extent of extracerebral pathology, which is present both ipsi- and contralaterally with respect to the primary lesion, and over large portions of the temporal, prefrontal, parietal and occipital lobes. Interestingly, the extent of extracerebral injuries is comparable in both hemispheres. Some edema is also found above the frontopolar area of the right hemisphere.

Figure 10 (C) displays non-hemorrhagic cerebral lesions. The primary lesion occupies a significant volumetric extent within the temporal lobe of the left hemisphere, with smaller lesions in the

frontopolar areas of both hemispheres as well as smaller, contre-coup lesions in the right temporal lobe. Figure 10 (D) reveals that some portions of these lesions are hemorrhagic, with significant bleeding in the left temporal lobe and in the frontal lobes.

Figure 11 showcases the results of segmenting the MR volumes acquired during the follow-up session. In the case of the ventricular system (Figure 11 (A)), as one might expect as due to partial recovery, there is considerably more lateral symmetry than in the acute case. Approximately eight months after acute injury, the lesion in the left temporal lobe is seen to have progressed into a structure (Figure 11 (B)) consisting of low-density WM and/or GM perfused by CSF. Diffuse bleeds are identified throughout the brain (Figure 11 (C)), mostly in areas which appear to hemorrhage in the acute baseline volume, though a few also appear in new locations (see arrows). Overall, the full model of the anatomy at follow-up (Figure 11 (D)) indicates noteworthy improvement after eight months of recovery and treatment.

Figure 12 shows the results of the longitudinal analysis for the third patient. In the case of the GM volume, surface displacement is visible in the acute baseline case compared to the follow-up case. For example, the view of the left hemisphere reveals this to be the case particularly in occipital, parietal and dorso-frontal areas, where the segmented GM surface for the acute baseline model (red) lies above the corresponding surface for the follow-up case (green). For the right hemisphere, the dorsal view of the GM models has large portions of the acute baseline volume lying atop the follow-up volume, and vice versa for the left hemisphere. This obviates a clear right-ward shift of the GM in the acute baseline case, presumably as a result of inflammation in the left temporal lobe. Confirmation of this impression is suggested by the ventral view of the brain, where it is seen that the temporal lobe and frontopolar regions are both larger in the acute baseline.

The longitudinal comparison of the WM volumes also indicates the presence of large differences between the two time points. The right and left views reveal a striped appearance of the two superposed models, with the crowns of gyri in the baseline volume consistently atop the corresponding gyral crowns in the follow-up volume, and vice versa for the troughs of gyri. This relative positioning of the two surfaces is consistent with the scenario of diffuse inflammation throughout the acute baseline WM volume, and possibly with the presence of DAI at the GM-WM boundary. In addition to these findings, the longitudinal WM analysis confirms the impressions formed from inspecting the GM volumes, where a general right-ward shift of the brain had been found. This scenario is confirmed by exploring the longitudinal comparison of the ventricular system where, in the acute baseline model, the left ventricle (ipsilateral to the primary insult) is positioned above the level corresponding to the follow-up model. This situation is reversed for the contralateral (right) hemisphere, suggesting a shearing transformation between the two models wherein the acute baseline brain mass is rotated counterclockwise about the antero-posterior axis as a result of the primary injury. This scenario is confirmed by the clear shift of the fourth ventricle in the acute baseline model (red) towards the left hemisphere, compared to the position of this ventricle in the follow-up model. Similar shifts are observed for the ventricular horns in the anterior and posterior views of Figure 12 (D).

As shown in Figure 12 (E), the longitudinal analysis of Patient 3 reveals significant decreases in the total volume of injured brain regions, especially with regard to frontal lobe lesions as well as microbleeds located diffusely throughout the brain. As outlined in Table 3, the former are found to have a combined volume that is significantly smaller at chronic follow-up (0.9 cm^3) than at acute baseline (54.7 cm^3). A similar impression emerges for hemorrhagic lesions (0.3 cm^3 at follow-up, 22.5 cm^3 at baseline).

Discussion

Significance

Neuroimaging has become extremely important for TBI surgical planning as well as for the provision of important prognostic indicators which may help the aggressiveness of injury management (Lee and Newberg 2005). Brain contusions are relatively common in TBI, occurring in a large fraction of patients with blunt trauma, frequently as coup or contre-coup injuries. Similarly, subdural hematomas occur in 10-20% of patients with head trauma and are associated with high mortality (50-85%) (Gutman, Moulton et al. 1992). Thus, intracranial hemorrhage detection of the type performed here is important in the process of identifying the mechanism of injury as well as the potential clinical outcome. Detection of micro-hemorrhages is dependent upon a large number of MR sequence parameters, including spatial resolution, slice thickness and TE (Greenberg, Vernooij et al. 2009). Because the SWI sequence as used here takes into account MR signal phase information, regional magnetic field alterations due to iron concentration gradients in the brain are easier to capture with this technique. As a result, the use of susceptibility weighted imaging is highly beneficial because susceptibility effects make micro-hemorrhages more obvious in SWI images compared to other paradigms.

The ability of the 3D Slicer environment presented here to identify and quantify DAI is significant because this type of pathology contributes to disability in approximately 40% of closed head injuries (Buki et al in Ding 2008). Moreover, the presence of hemorrhage in DAI lesions may portend a poor prognosis compared to their absence (Paterakis, Karantanas et al. 2000; Pierallini, Pantano et al. 2000). Thus, the ability to differentiate between hemorrhagic and non-hemorrhagic edema using 3D Slicer may be of critical use to clinicians in their attempts to evaluate the extent of each type of edema, and to formulate appropriate forms of treatment or critical care. In addition, because the number of traumatic microbleeds detected chronically in T2-weighted GRE and SWI images is significantly correlated with Glasgow Coma Scale (GCS) and Extended Glasgow Outcome Scale (GOS-E) scores, respectively (Itti, Chang et al. 2001; Tong, Ashwal et al. 2008), the capabilities of this imaging and visualization environment are well-suited for the analysis of TBI data in view of exploring the relationship between information provided by neuroimaging techniques and results from neuropsychological testing.

Various quantitative measures that can be extracted from MR images using segmentation methods have been correlated with clinical outcome measures. For example, total lesion volume in TBI as extracted from FLAIR images has been found to correlate significantly with clinical scores (Pierallini, Pantano et al. 2000). Because the signal that arises from CSF is suppressed in FLAIR imaging, more precise estimation of parenchymal damage is possible using this type of sequence. Similarly, a study of 69 TBI patients found a stepwise, dose-response relationship between parenchymal volume loss and TBI severity (Levine, Kovacevic et al. 2008) and concluded that patterns of parenchymal volumetric changes can differentiate among levels of TBI severity, even in mild TBI. Using the 3D Slicer environment and the type of analysis described in this paper to perform TBI quantification can be useful in such studies to compute volumetric measures as well as to obtain results comparable to those of manual analysis methods.

Comparison with previous work

Present segmentation results are consistent with the previous finding that approximately half of DAI lesions are located either in the deep WM or at the cortico-medullary junction (GM-WM interface) of the frontal and temporal lobes (Adams, Graham et al. 1982). In this respect, our case studies illustrate findings that are quite typical of TBI pathology and thus very well-suited for demonstrating the segmentation and analysis capabilities of the 3D Slicer environment. The large lesions that are both

hyperintense in FLAIR images and superficial with respect to the cortical surface of this patient are also typical of TBI pathology, as they involve the frontal and temporal lobes (Pierallini, Pantano et al. 2000). One improvement of the present approach over previous studies consists of the superior multimodal ability to identify, distinguish and characterize hemorrhagic vs. nonhemorrhagic lesions. In this respect, sensitivity and specificity may be comparable to those of investigations which found improved detection of hemorrhage using SWI as compared to other studies which did not benefit from the availability of this technique (Tong, Ashwal et al. 2003; Tong, Ashwal et al. 2008).

Numerous studies have identified MRI-extracted correlates between TBI pathology and neuropsychological outcomes in the areas of information processing speed, learning and memory, as well as executive function. In particular, GM volume has been strongly linked to chronic damage to WM tracts (Warner, Marquez de la Plata et al. 2010). Similarly, changes in WM and GM volume were found to correlate well with functional TBI outcome as measured using the Functional Status Examination (FSE) and FLAIR-measured acute axonal lesions are strongly predictive of post-traumatic cerebral atrophy (Ding, Marquez de la Plata et al. 2008), which can also be quantified using the metrics previously described (bifrontal index, bicaudate index, etc.). In addition, global brain volume loss correlates well with admission GCS, coma duration and amnesia (Ding, Marquez de la Plata et al. 2008), and total lesion volume as measured two to three months after injury using FLAIR correlates significantly with the 1-year Glasgow Outcome Score (GOS) (Pierallini, Pantano et al. 2000). These analyses are reproducible and can be streamlined using the 3D Slicer environment, particularly as a consequence of the latter's ability to extract brain volumetrics straightforwardly and to perform longitudinal intra-subject analysis. For example, cortical brain volumes are suggestive of learning, memory, and processing speed performance (Warner, Marquez de la Plata et al. 2010); similarly, total brain volume loss has been associated with loss of consciousness duration (MacKenzie, Siddiqi et al. 2002). Thus, the 3D Slicer environment can be of particular interest to researchers who quantify TBI using measures of these cognitive functions.

It has been suggested that lesion volume in acute DAI can be used to stratify injury severity when selecting patients for TBI clinical trials (Ding, Marquez de la Plata et al. 2008). Thus, the ability of the 3D Slicer environment to offer useful information on DAI pathological change might be useful for DAI-directed therapies. A study involving 37 TBI patients found a mean decrease in brain volume of -1.43% between about 79 and 409 days post-TBI, with greater decline in brain volume being associated with longer duration of post-injury coma (Trivedi, Ward et al. 2007); the findings of our volumetric analysis are comparable to these results as well as to those of Sidaros et al. (Sidaros, Skimminge et al. 2009), who found a %BVC ranging between -0.6% and -9.4% (mean of -4.0%) in a population of 24 TBI patients. For our three cases, the %BVC was found to have a mean of -10.3% and a standard deviation of 1.89% (Table 3). Although in our study the sample size is very small, these percentage changes in brain volume appear to be in line with previous %BVC ranges, especially given the extreme TBI severity being investigated in this paper. In conclusion, because cerebral atrophy is known to reach significance 8-12 months after the traumatic event (Blatter 97 in Ding). (Blatter, Bigler et al. 1997), we expect that the cases described in this article may be reasonably representative of the typical atrophy patterns observed in TBI populations.

Conclusion

As demonstrated here, 3D Slicer offers dramatic improvement over existing analysis tools for the purpose of TBI analysis. Specifically, through the use of this freely available environment, multimodal registration and bias field correction of an unlimited number of MR volumes acquired using different sequences can be accomplished. In addition to this, semi-automatic use of ABC as well as of other

segmenters available through 3D Slicer allows one to perform highly robust tissue classification and 3D model generation. The calculation of anatomic measures (such as volume and area) associated with structures of interest is not only of high clinical relevance, but also methodologically straightforward. In conclusion, we expect 3D Slicer as well as the type of quantitative analysis illustrated here to have significant impact upon the state of the art in TBI neuroimaging as well as upon the added benefit of neuroimaging from the standpoint of TBI monitoring and treatment.

Acknowledgment

We acknowledge the assistance of Silvain Gouttard, Bo Wang, Steve Pieper, David McArthur, Maria Echeparre, Stephen Aylward, Sonja Pujol and the staff of the Laboratory of Neuro Imaging at UCLA. 3D Slicer is a multi-platform, free and open source software package for visualization and medical image computing available from www.slicer.org. This work was supported by the National Alliance for Medical Image Computing (NA-MIC; www.na-mic.org), under NIH Roadmap Initiative grant 2U54EB005149 to R. K. and sub-award to J. D. V. H.

References

- Adams, J. H., D. I. Graham, et al. (1982). "Diffuse axonal injury due to nonmissile head injury in humans: an analysis of 45 cases." Ann Neurol **12**(6): 557-563.
- Bates, E., S. M. Wilson, et al. (2003). "Voxel-based lesion-symptom mapping." Nat Neurosci **6**(5): 448-450.
- Blatter, D. D., E. D. Bigler, et al. (1997). "MR-based brain and cerebrospinal fluid measurement after traumatic brain injury: correlation with neuropsychological outcome." AJNR Am J Neuroradiol **18**(1): 1-10.
- Chen, A. J. and M. D'Esposito (2010). "Traumatic brain injury: from bench to bedside [corrected] to society." Neuron **66**(1): 11-14.
- Chesnut, R. M. (1998). "Implications of the guidelines for the management of severe head injury for the practicing neurosurgeon." Surg Neurol **50**(3): 187-193.
- De Beaumont, L., H. Theoret, et al. (2009). "Brain function decline in healthy retired athletes who sustained their last sports concussion in early adulthood." Brain **132**(Pt 3): 695-708.
- De Coene, B., J. Hajnal, et al. (1992). "MR of the brain using fluid-attenuated inversion recovery (FLAIR) pulse sequences." AJNR Am J Neuroradiol **13**(6): 1555-1564.
- Ding, K., C. Marquez de la Plata, et al. (2008). "Cerebral atrophy after traumatic white matter injury: correlation with acute neuroimaging and outcome." J Neurotrauma **25**(12): 1433-1440.
- Dubroff, J. G. and A. Newberg (2008). "Neuroimaging of traumatic brain injury." Semin Neurol **28**(4): 548-557.
- Earnest, M. P., R. K. Heaton, et al. (1979). "Cortical atrophy, ventricular enlargement and intellectual impairment in the aged." Neurology **29**(8): 1138-1143.
- Faul M., X. L., Wald M.M., Coronado V.G. (2010). Traumatic Brain Injury in the United States: Emergency Department Visits, Hospitalizations and Deaths 2002-2006. Atlanta, GA, Centers for Disease Control and Prevention, National Center for Injury Prevention and Control.
- Filippi, M., Gawne-Cain, ML., Gasterini, C. (1998). "Effect of training and different measurement strategies on the reproducibility of brain MRI lesion load measurements in multiple sclerosis." Neurology **50**: 238-244.
- Greenberg, S. M., M. W. Vernooij, et al. (2009). "Cerebral microbleeds: a guide to detection and interpretation." Lancet Neurol **8**(2): 165-174.
- Gutman, M. B., R. J. Moulton, et al. (1992). "Risk factors predicting operable intracranial hematomas in head injury." J Neurosurg **77**(1): 9-14.
- Gyldensted, C. (1977). "Measurements of the normal ventricular system and hemispheric sulci of 100 adults with computed tomography." Neuroradiology **14**(4): 183-192.
- Hahn, F. J. and R. L. Schapiro (1976). "The excessively small ventricle on computed axial tomography of the brain." Neuroradiology **12**(3): 137-139.
- Huckman, M. S., J. Fox, et al. (1975). "Validity of Criteria for Evaluation of Cerebral Atrophy by Computed Tomography." Radiology **116**(1): 85-92.
- Huisman, T. A. (2003). "Diffusion-weighted imaging: basic concepts and application in cerebral stroke and head trauma." Eur Radiol **13**(10): 2283-2297.
- Huisman, T. A., A. G. Sorensen, et al. (2003). "Diffusion-weighted imaging for the evaluation of diffuse axonal injury in closed head injury." J Comput Assist Tomogr **27**(1): 5-11.
- Itti, L., L. Chang, et al. (2001). "Segmentation of progressive multifocal leukoencephalopathy lesions in fluid-attenuated inversion recovery magnetic resonance imaging." J Neuroimaging **11**(4): 412-417.
- Jones, K. M., R. V. Mulkern, et al. (1992). "Fast spin-echo MR imaging of the brain and spine: current concepts." AJR Am J Roentgenol **158**(6): 1313-1320.

- Langlois, J. A., Rutland-Brown, W., Thomas, K. Traumatic brain injury in the United States: emergency department visits, hospitalizations, and deaths. Atlanta, GA, National Center for Injury Prevention and Control.
- Lee, B. and A. Newberg (2005). "Neuroimaging in traumatic brain imaging." NeuroRx **2**(2): 372-383.
- Levine, B., N. Kovacevic, et al. (2008). "The Toronto traumatic brain injury study: injury severity and quantified MRI." Neurology **70**(10): 771-778.
- MacKenzie, J. D., F. Siddiqi, et al. (2002). "Brain atrophy in mild or moderate traumatic brain injury: a longitudinal quantitative analysis." AJNR Am J Neuroradiol **23**(9): 1509-1515.
- Maes, F., A. Collignon, et al. (1997). "Multimodality image registration by maximization of mutual information." IEEE Trans Med Imaging **16**(2): 187-198.
- Mugler, J. P., 3rd and J. R. Brookeman (1990). "Three-dimensional magnetization-prepared rapid gradient-echo imaging (3D MP RAGE)." Magn Reson Med **15**(1): 152-157.
- Paterakis, K., A. H. Karantanas, et al. (2000). "Outcome of patients with diffuse axonal injury: the significance and prognostic value of MRI in the acute phase." J Trauma **49**(6): 1071-1075.
- Pierallini, A., P. Pantano, et al. (2000). "Correlation between MRI findings and long-term outcome in patients with severe brain trauma." Neuroradiology **42**(12): 860-867.
- Pohl, K. M., S. Bouix, et al. (2007). "A hierarchical algorithm for MR brain image parcellation." IEEE Trans Med Imaging **26**(9): 1201-1212.
- Prastawa, M., E. Bullitt, et al. (2009). "Simulation of brain tumors in MR images for evaluation of segmentation efficacy." Med Image Anal **13**(2): 297-311.
- Prastawa, M., E. Bullitt, et al. (2004). "A brain tumor segmentation framework based on outlier detection." Med Image Anal **8**(3): 275-283.
- Prastawa, M., E. Bullitt, et al. (2003). "Automatic brain tumor segmentation by subject specific modification of atlas priors." Acad Radiol **10**(12): 1341-1348.
- Prastawa, M., Gerig, G. (2008). "Brain lesion segmentation through physical model estimation." Lecture Notes in Computer Science **5358**: 562-571.
- Scheid, R., C. Preul, et al. (2003). "Diffuse axonal injury associated with chronic traumatic brain injury: evidence from T2*-weighted gradient-echo imaging at 3 T." AJNR Am J Neuroradiol **24**(6): 1049-1056.
- Sehgal, V., Z. Delproposto, et al. (2005). "Clinical applications of neuroimaging with susceptibility-weighted imaging." J Magn Reson Imaging **22**(4): 439-450.
- Sidaros, A., A. Skimminge, et al. (2009). "Long-term global and regional brain volume changes following severe traumatic brain injury: a longitudinal study with clinical correlates." Neuroimage **44**(1): 1-8.
- Synek, V., J. R. Reuben, et al. (1976). "Comparing Evans' index and computerized axial tomography in assessing relationship of ventricular size to brain size." Neurology **26**(3): 231-233.
- Taber, K. H., D. L. Warden, et al. (2006). "Blast-related traumatic brain injury: what is known?" J Neuropsychiatry Clin Neurosci **18**(2): 141-145.
- Tong, K. A., S. Ashwal, et al. (2003). "Hemorrhagic shearing lesions in children and adolescents with posttraumatic diffuse axonal injury: improved detection and initial results." Radiology **227**(2): 332-339.
- Tong, K. A., S. Ashwal, et al. (2008). "Susceptibility-weighted MR imaging: a review of clinical applications in children." AJNR Am J Neuroradiol **29**(1): 9-17.
- Trivedi, M. A., M. A. Ward, et al. (2007). "Longitudinal changes in global brain volume between 79 and 409 days after traumatic brain injury: relationship with duration of coma." J Neurotrauma **24**(5): 766-771.
- Unterberg, A. W., J. Stover, et al. (2004). "Edema and brain trauma." Neuroscience **129**(4): 1021-1029.

- Van Leemput, K., F. Maes, et al. (1999). "Automated model-based tissue classification of MR images of the brain." IEEE Trans Med Imaging **18**(10): 897-908.
- Warach, S., J. Gaa, et al. (1995). "Acute human stroke studied by whole brain echo planar diffusion-weighted magnetic resonance imaging." Ann Neurol **37**(2): 231-241.
- Warner, M. A., C. Marquez de la Plata, et al. (2010). "Assessing spatial relationships between axonal integrity, regional brain volumes, and neuropsychological outcomes after traumatic axonal injury." J Neurotrauma **27**(12): 2121-2130.
- Watts, D. D., D. Hanfling, et al. (2004). "An evaluation of the use of guidelines in prehospital management of brain injury." Prehosp Emerg Care **8**(3): 254-261.
- Zoellei, L., Shenton, M., Wells, W., Pohl, K. (2007). The impact of atlas formation methods on atlas-guided brain segmentation. International Conference on Medical Image Computing and Computer Assisted Intervention (MICCAI). **10**: 39-46.

Figure Captions

Figure 1. Sample MR images acquired from Patient 1 using the standard protocol. The first and second columns contains images acquired at acute baseline and chronic follow-up, respectively. Shown from top to bottom are T1-weighted MP-RAGE images (A), T2-weighted TSE (B), FLAIR (C), T2-weighted GRE (D) and SWI (E). Arrows are color coded to represent the following: red—primary lesion(s), blue—smaller lesion(s), green—micro-hemorrhage(s); yellow—DAI. Note that only representative (i.e. not all) injuries of each type are indicated by arrows.

Figure 2. Three-dimensional models of TBI anatomy for Patient 1 (acute baseline time point), as generated in 3D Slicer. Each row displays one of six canonical views of the brain, whereas each column corresponds to a structure type (ventricles, extracerebral injuries, non-hemorrhagic lesions, hemorrhagic lesions, and full model). The GM and WM volumes are shown as transparent to facilitate visualization of each structure in relationship to cortical landmarks. In (B)-(E), ventricles are also shown as transparent for similar reasons. Arrows indicate TBI-related pathology of interest (see text for elaboration).

Figure 3. As in Figure 2, for the chronic follow-up time point.

Figure 4. Longitudinal analysis of TBI in Patient 1 using 3D Slicer-generated volumes displayed in red (for the acute baseline time point), or green (for the chronic follow-up time point). As in Figures 2-3, each row displays one of six canonical views of the brain, with WM and GM transparent in (C)-(D) to facilitate visualization of each structure in relationship to cortical landmarks.

Figure 5. As in Figure 1, for Patient 2.

Figure 6. As in Figure 2, for Patient 2 at the acute baseline time point.

Figure 7. As in Figure 2, for Patient 2 at the chronic follow-up time point.

Figure 8. As in Figure 4, for Patient 2.

Figure 9. As in Figure 1, for Patient 3.

Figure 10. As in Figure 2, for Patient 3 at the acute baseline time point.

Figure 11. As in Figure 2, for Patient 3 at the chronic follow-up time point.

Figure 12. As in Figure 3, for Patient 3.

Patient	Age	Sex	Cause of injury	Day of acute scan	Day of chronic scan	T1 pre-contrast	T2 TSE	FLAIR	GRE T2	SWI	Perfusion	T1 post-contrast	OEF EP SE	DTI	DWI 1	DWI 2	mIP
1	45	M	blunt trauma	2	176	✓	✓	✓	✓	✓							
2	31	M	gun shot	2	201	✓	✓	✓	✓	✓							
3	33	M	blunt trauma	3	238	✓	✓	✓	✓	✓	✓	✓	✓	✓	✓	✓	✓

Table 1. Case study subject data specifying the age, sex, cause of injury, dates of scanning sessions as well as MR modalities acquired from each TBI study case. Scanning session dates are specified as the number of days after acute injury when the acute and chronic MR volumes were acquired, respectively. Check marks indicate use of each MR scan type (see text for clarification).

Sequence	parameter									
	TR [ms]	TE [ms]	TI [ms]	FA [deg]	ETL	thickness [mm]	phase FOV [%]	sampling [%]	acquisition type	matrix
pre-contrast T1	1900	3.52	900	9	1	1	100	100	3D	256 x 256
T2 TSE	3330	89		120	18	5	100	75	2D	512 x 512
FLAIR	8000	70	2375	130	16	3	75	75	2D	384 x 512
GRE T2	1500	7		20	1	3	75	80	2D	384 x 512
SWI	27	20		15	1	1.5	75	95	3D	192 x 256
Perfusion	2000	32		90	1	6	100	100	2D	128 x 128
post-contrast T1	1900	3.52	900	9	1	1	100	100	3D	256 x 256
OEF EP SE	10000	50		90	1	3	100	100	2D	128 x 128
DTI	8000	95		90	1	3	100	100	2D	128 x 128
DWI 1	4000	80		90	1	6	100	100	2D	130 x 130
DWI 2	4000	80		90	1	6	100	100	2D	130 x 130
mIP	27	20		15	1	12	75	95	3D	256 x 192

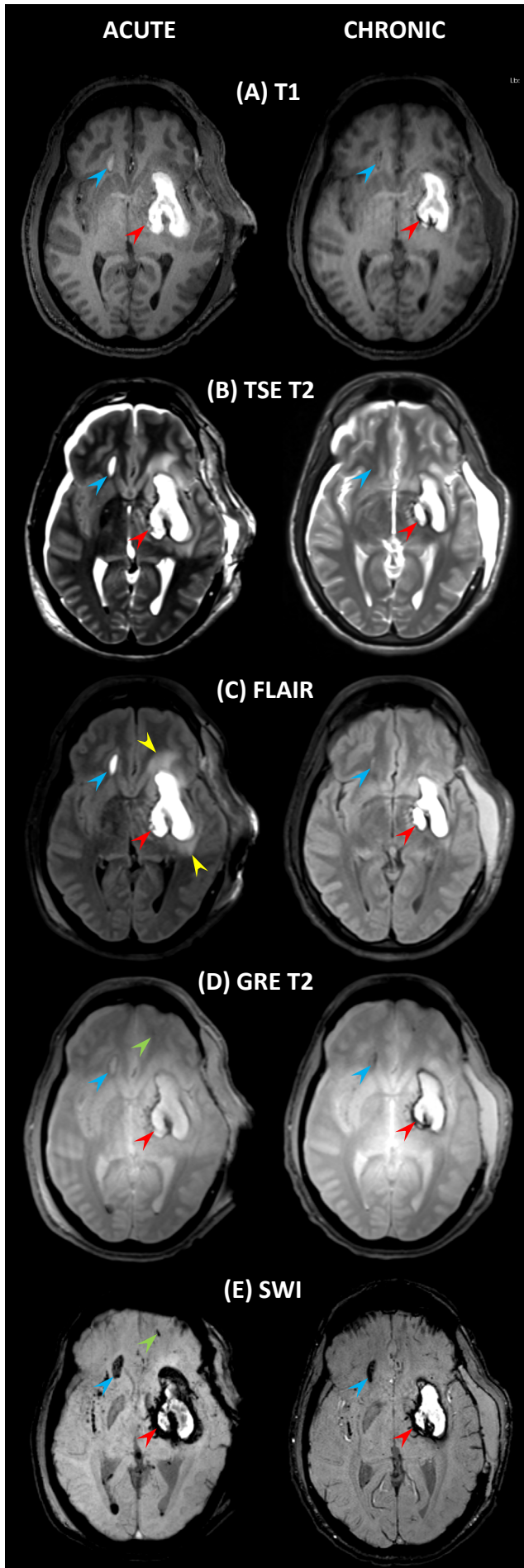
Table 2. Standard MR acquisition parameters associated with each sequence type specified in Table 1. Abbreviations: TR = repetition time; TE = echo time; TI = inversion time; FA = flip angle; ETL = echo train length; TSE = turbo spin echo; FLAIR = fluid-attenuated inversion recovery; GRE = gradient recalled echo; SWI = susceptibility-weighted imaging; OEF = oxygen extraction fraction; EP = echo-planar; SE = spin echo; DTI = diffusion tensor imaging; DWI = diffusion weighted imaging; mIP = maximum intensity projection.

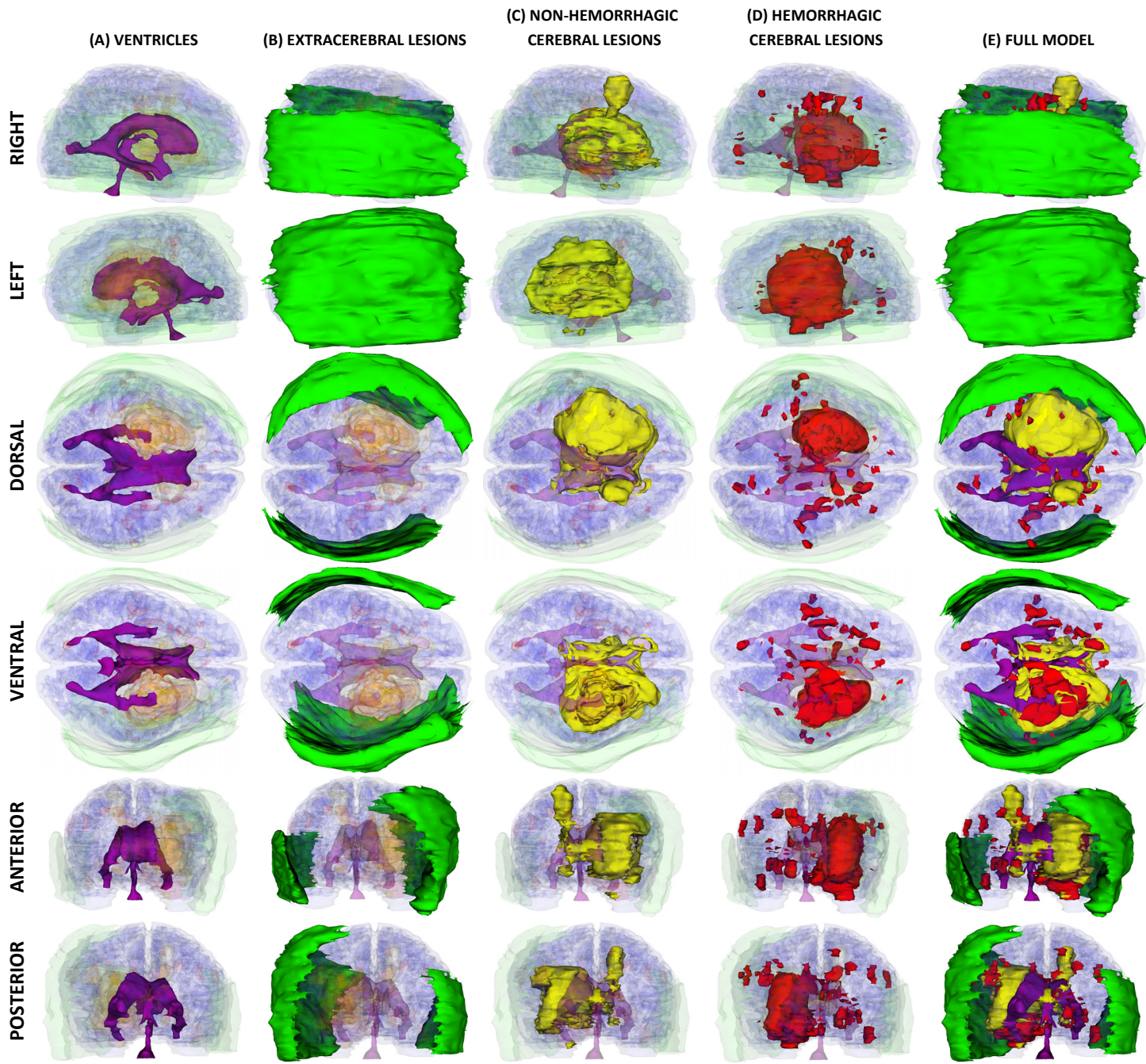
structure	patient	volume [cm ³]		Δ [%]
		acute	chronic	
brain	1	1142.0	1009.3	-11.6
	2	1098.5	978.7	-10.9
	3	1111.2	1018.1	-8.4
ventricular system	1	29.7	30.1	1.3
	2	45.8	95.2	107.6
	3	20.5	31.4	53.2
non-hemorrhagic lesions	1	84.7	19.9	-76.5
	2	40.7	14.8	-63.6
	3	54.7	0.9	-82.7
hemorrhagic lesions	1	73.0	17.4	-76.2
	2	51.3	<0.1	-99.7
	3	22.5	0.3	-88.1

Table 3. Longitudinal analysis of three selected volumetric structures (ventricular system, non-hemorrhagic lesions and hemorrhagic lesions) in three TBI patients. Values are reported for both acute and chronic segmented volumes, with the change Δ as a percentage being computed as (volume at the chronic time point — volume at the acute time point) × 100 / volume at the acute time point.

metric	patient	time point		Δ [%]	μ (Δ) [%]	σ (Δ) [%]
		acute	chronic			
HLV [cm]	1	2.323	2.541	9.63	6.63	4.97
	2	2.965	2.985	0.89		
	3	3.077	3.364	9.35		
MLV [cm]	1	0.541	0.554	2.41	19.32	18.67
	2	0.845	0.983	16.19		
	3	0.765	1.067	39.36		
MISD [cm]	1	14.546	14.313	-1.60	0.44	2.68
	2	14.068	13.960	-0.55		
	3	13.209	13.669	3.48		
bifrontal index	1	0.205	0.217	5.76	6.23	0.40
	2	0.250	0.266	6.40		
	3	0.251	0.267	6.51		
bicaudate index	1	0.047	0.046	-3.72	25.44	28.47
	2	0.068	0.086	26.89		
	3	0.059	0.091	53.17		
Evan's index	1	0.159	0.177	11.42	6.18	5.00
	2	0.211	0.214	1.46		
	3	0.233	0.246	5.67		
ventricular index	1	0.233	0.218	-6.58	12.01	17.23
	2	0.286	0.329	15.16		
	3	0.249	0.317	27.44		
Huckman's index	1	28.587	30.949	8.27	9.30	5.59
	2	38.054	39.688	4.30		
	3	38.430	44.321	15.33		

Table 4. Indices of atrophy computed for three sample subjects. In addition to the numerical values of each parameter, also listed is the change Δ as a percentage, computed as $(\text{value at chronic time point} - \text{value at acute time point}) \times 100 / \text{value at acute time point}$. The mean μ and standard deviation σ of the percentage change Δ computed over subjects are also listed. Abbreviations: HLV = maximum width of the anterior horns of the lateral ventricles; MLV = minimum width of the lateral ventricles; MISD = maximum inner skull diameter.



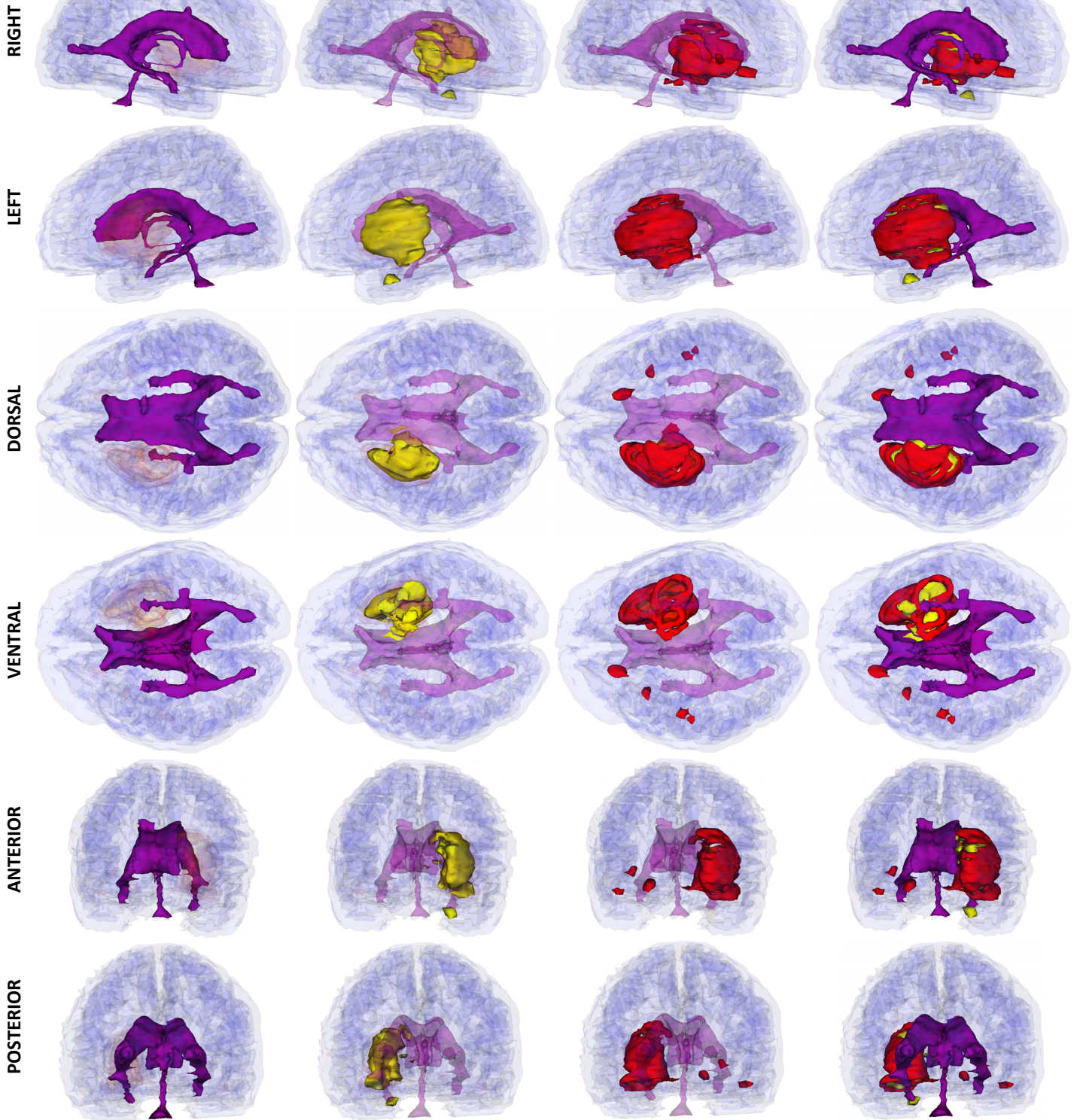


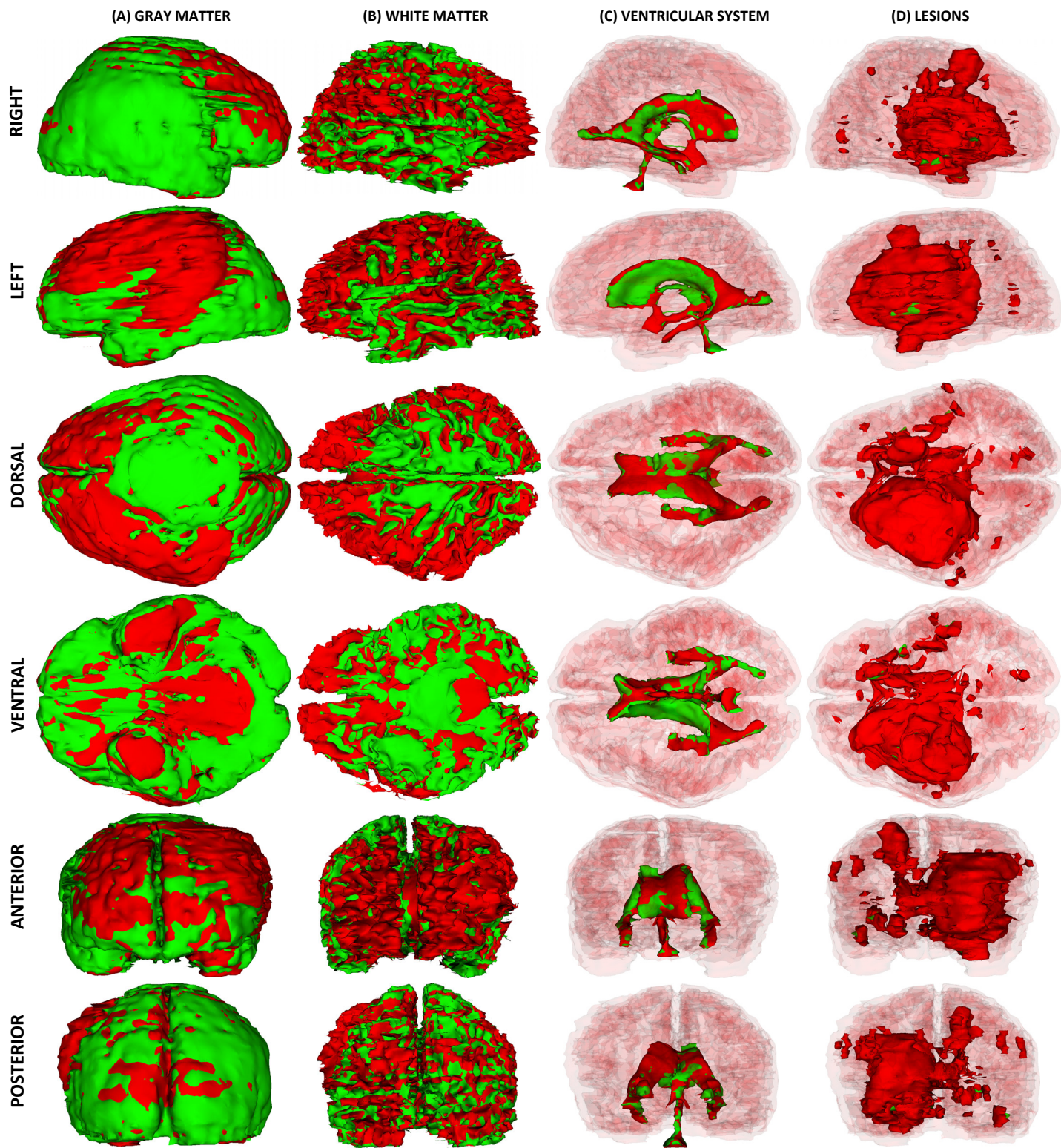
(A) VENTRICLES

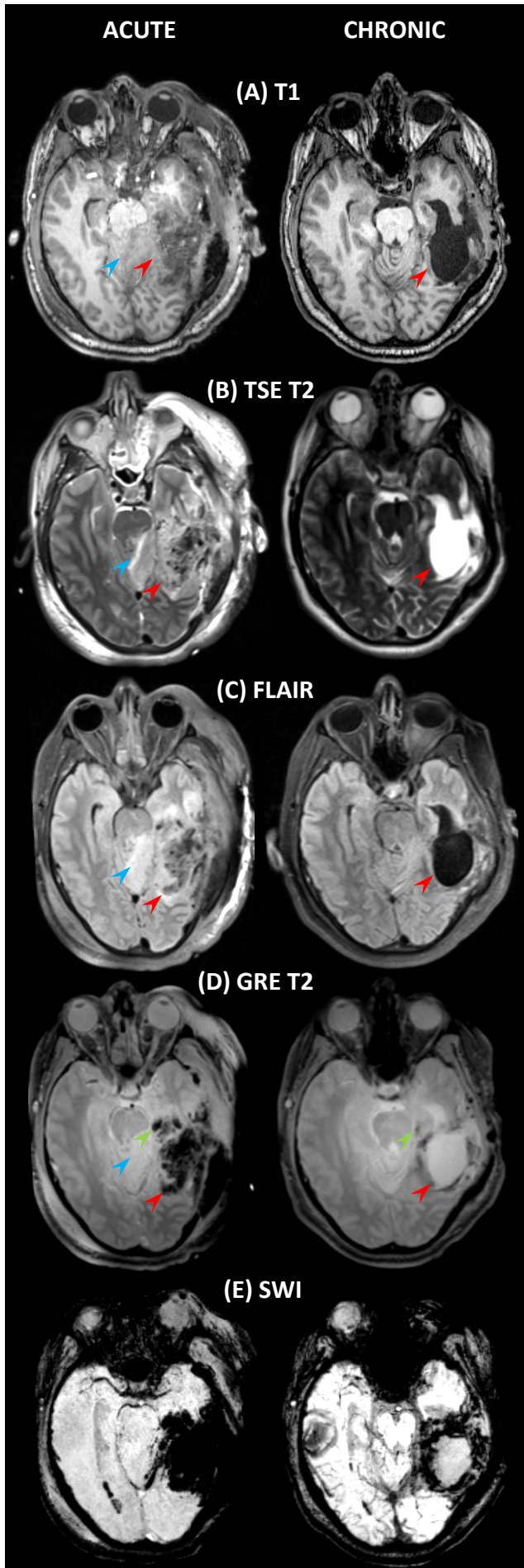
(B) LESIONS

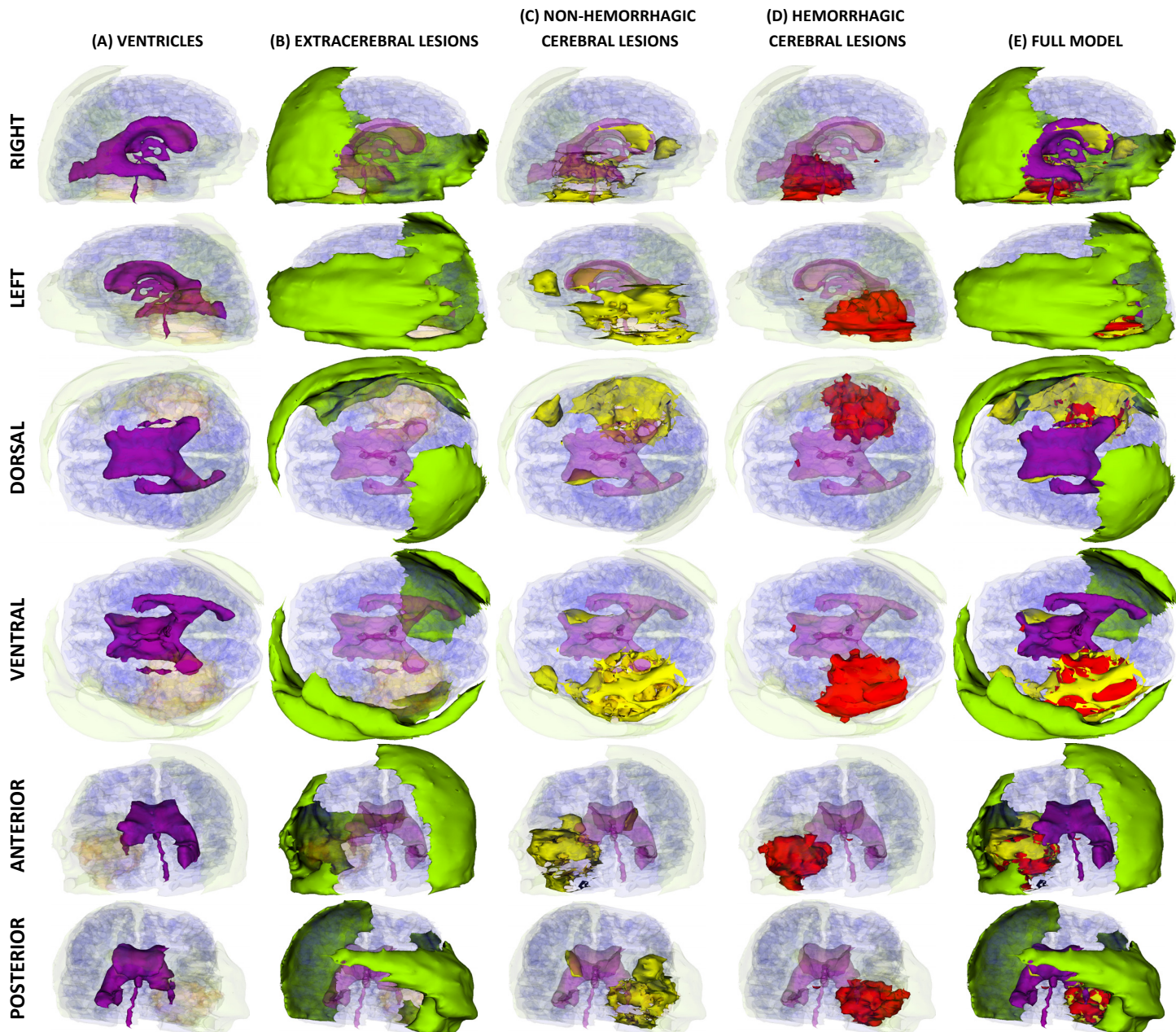
(C) BLEEDS

(D) FULL MODEL







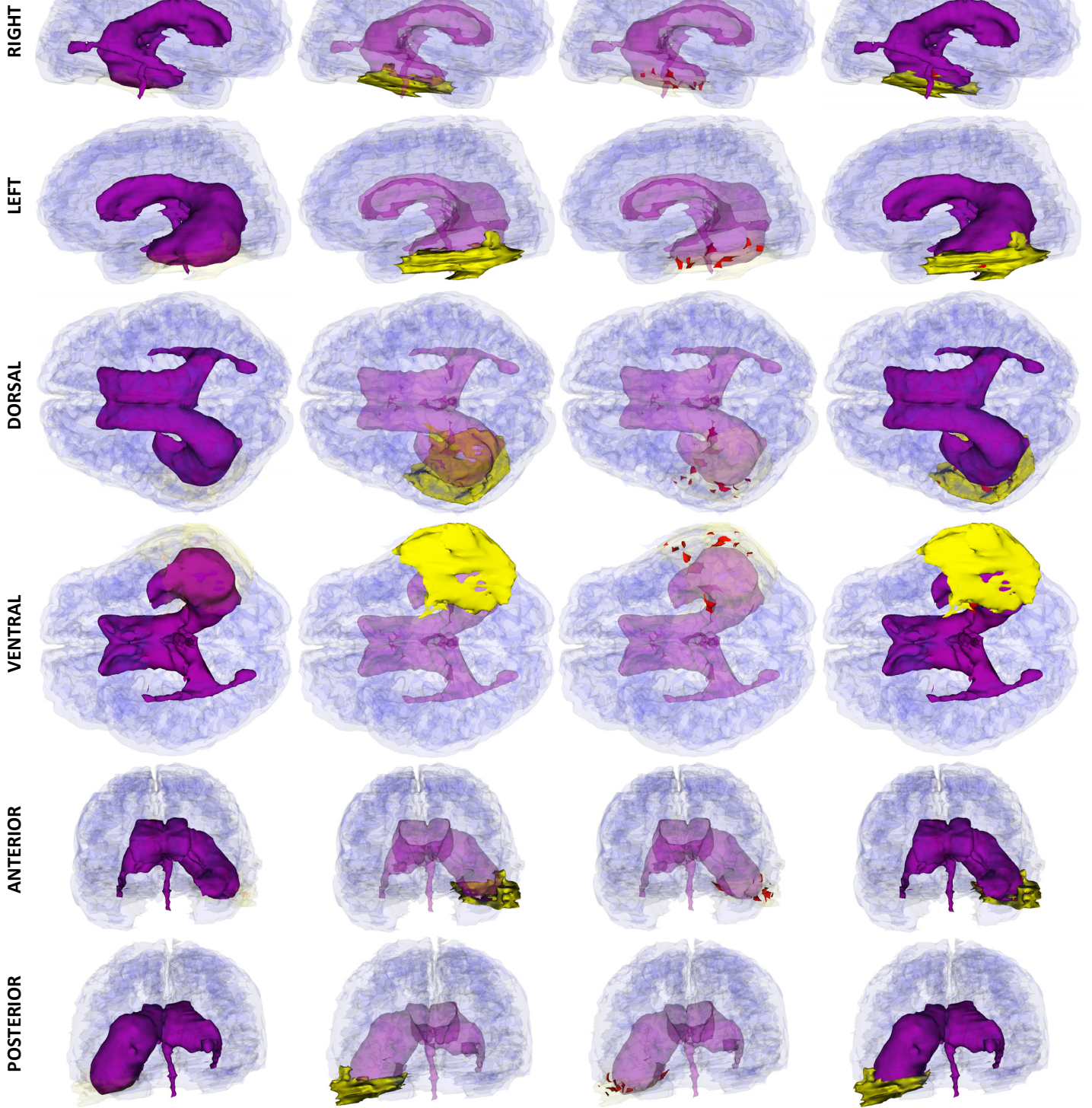


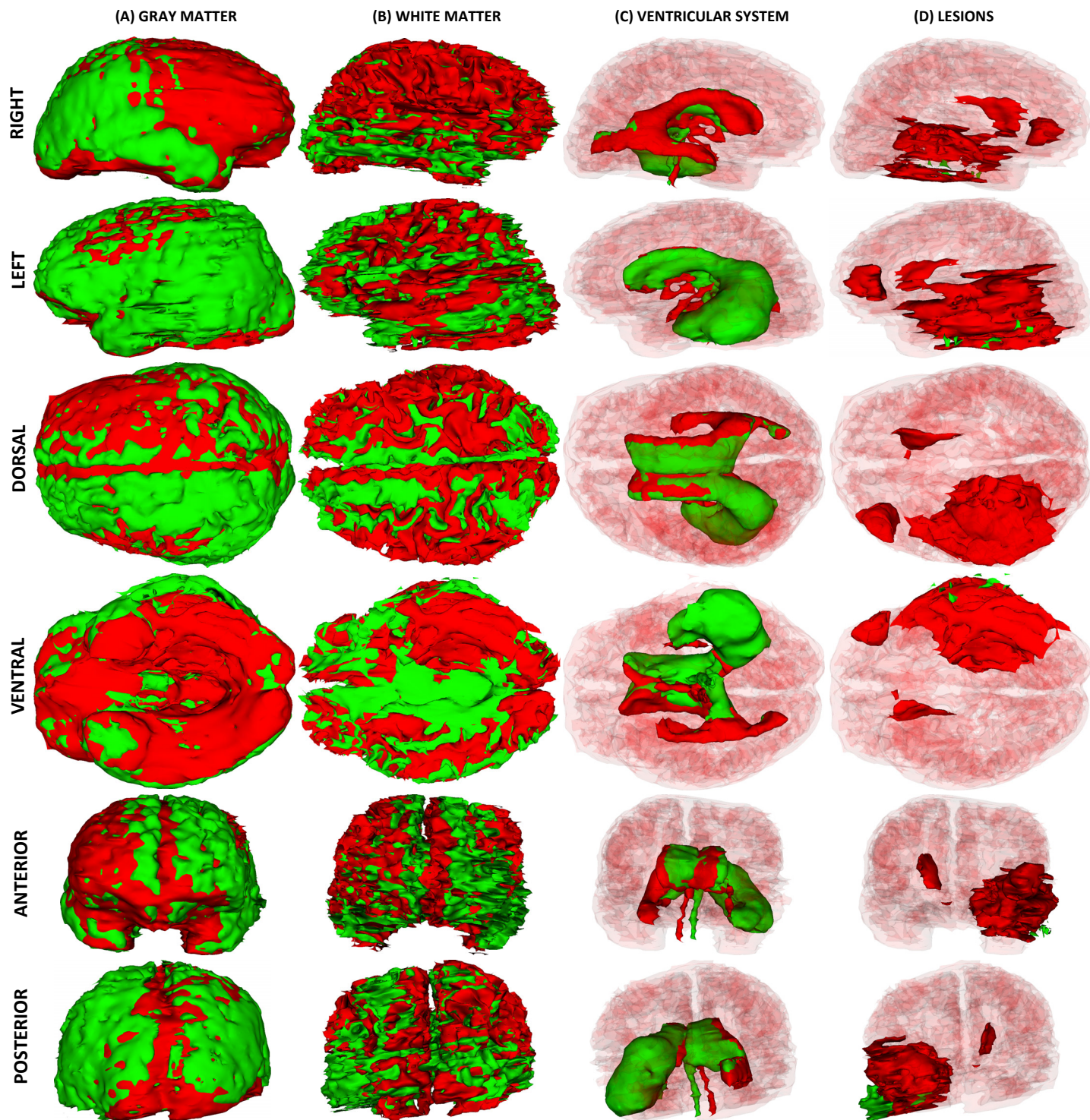
(A) VENTRICLES

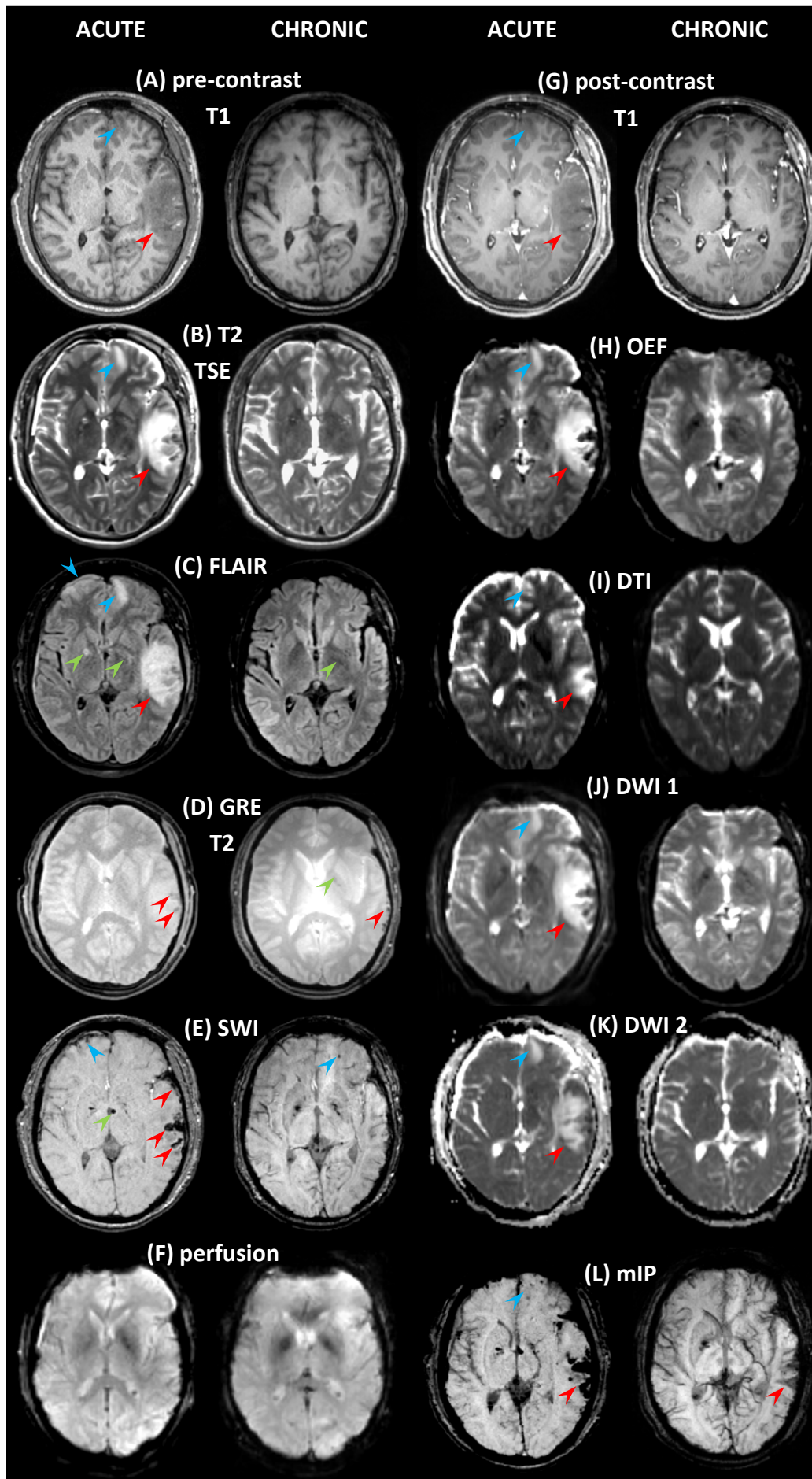
(B) LESIONS

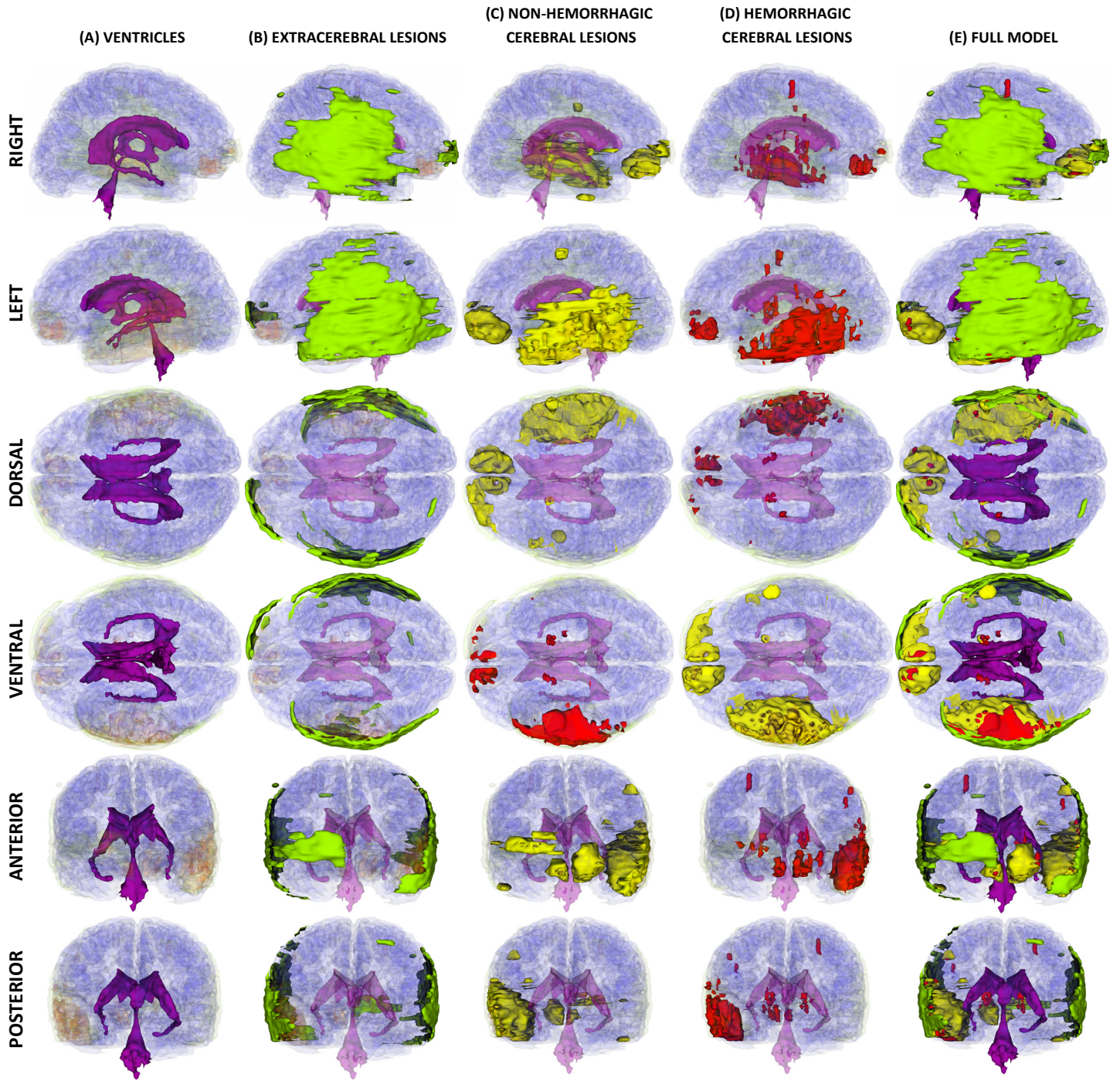
(C) BLEEDS

(D) FULL MODEL









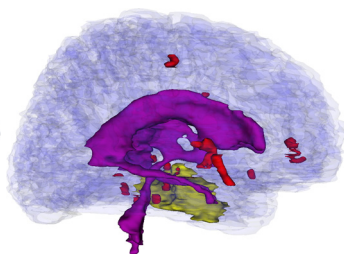
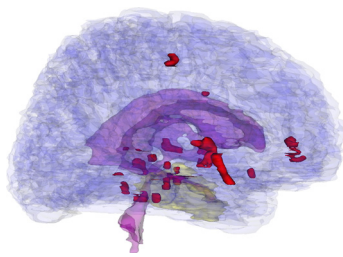
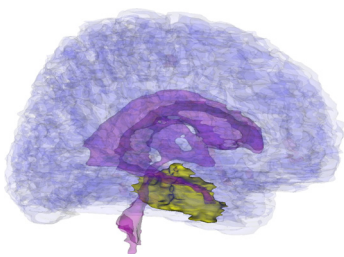
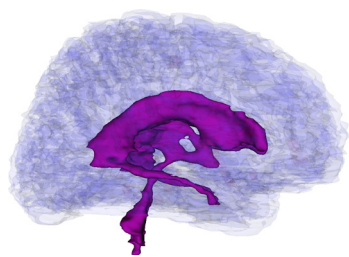
(A) VENTRICLES

(B) LESIONS

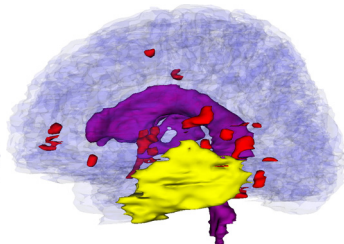
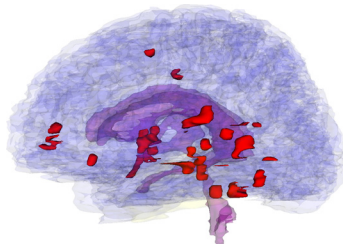
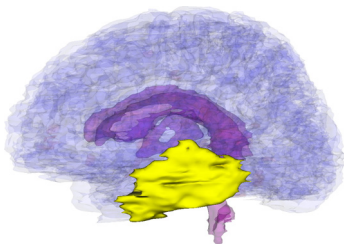
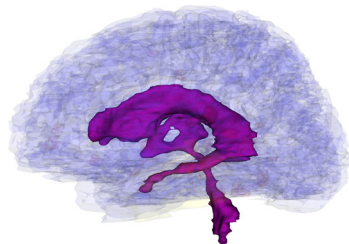
(C) BLEEDS

(D) FULL MODEL

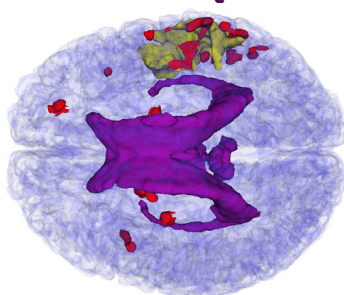
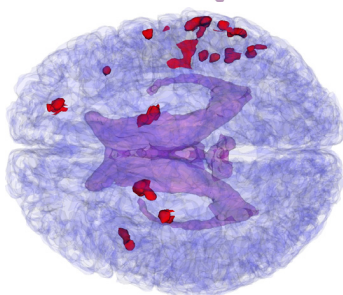
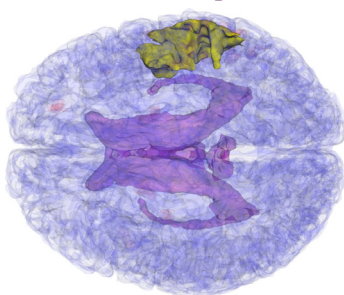
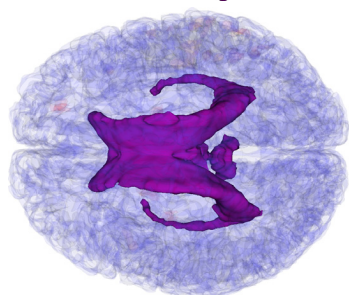
RIGHT



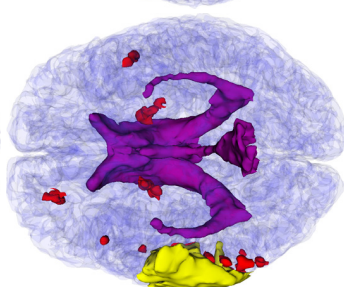
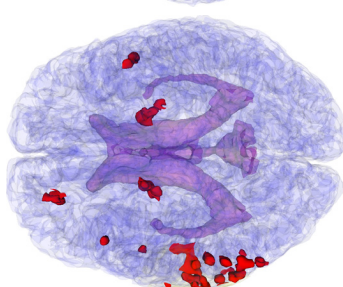
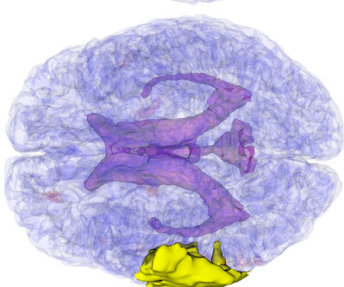
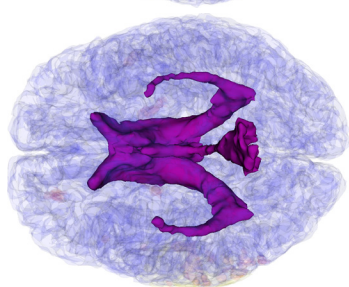
LEFT



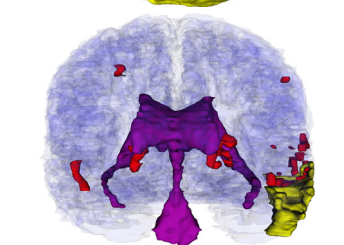
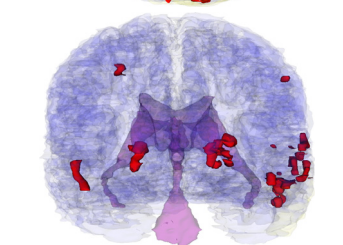
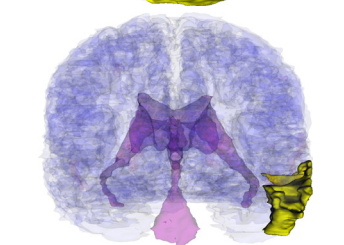
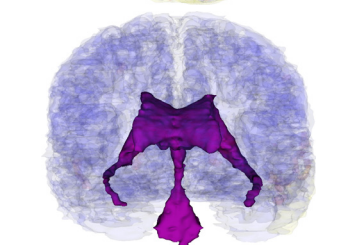
DORSAL



VENTRAL



ANTERIOR



POSTERIOR

